

Full paper

# $\alpha$ -MoO<sub>3-x</sub> by plasma etching with improved capacity and stabilized structure for lithium storage

Guobin Zhang<sup>a,1</sup>, Tengfei Xiong<sup>a,1</sup>, Mengyu Yan<sup>b</sup>, Liang He<sup>a,c</sup>, Xiaobin Liao<sup>a</sup>, Chunqing He<sup>d</sup>, Chongshan Yin<sup>d</sup>, Haining Zhang<sup>e</sup>, Liqiang Mai<sup>a,\*</sup>

<sup>a</sup> State Key Laboratory of Advanced Technology for Materials Synthesis and Processing, International School of Materials Science and Engineering, Wuhan University of Technology, Wuhan 430070, China

<sup>b</sup> Department of Materials Science and Engineering, University of Washington, Seattle, WA 98195, USA

<sup>c</sup> Department of Materials Science and NanoEngineering, Rice University, Houston, TX 77005, USA

<sup>d</sup> Key Laboratory of Nuclear Solid State Physics Hubei Province, School of Physics and Technology, Wuhan University, Wuhan 430072, China

<sup>e</sup> State Key Laboratory of Advanced Technology for Materials Synthesis and Processing, School of Materials Science and Engineering, Wuhan University of Technology, Wuhan 430070, China

## ARTICLE INFO

## Keywords:

Oxygen vacancy  
Molybdenum trioxide  
Cathode material  
Lithium-ion battery

## ABSTRACT

Compared with most cathodes for lithium-ion batteries (LIBs),  $\alpha$ -MoO<sub>3</sub> exhibits high specific capacity and therefore receives widespread attention. However, due to its irreversible structural transformation, the capacity of  $\alpha$ -MoO<sub>3</sub> declines rapidly upon discharge-charge process. Herein, via H<sub>2</sub> plasma etching, oxygen-deficient  $\alpha$ -MoO<sub>3-x</sub> with improved electrochemical performance is prepared on the basis of pristine  $\alpha$ -MoO<sub>3</sub> (MoO<sub>3</sub> (I)). The obtained MoO<sub>3</sub> (II) (10 min etching) and MoO<sub>3</sub> (III) (20 min etching) have reduced bandgap and expanded van der Waals gap (vdW gap). Electrochemical test results demonstrate MoO<sub>3</sub>(II) obtains the largest Li<sup>+</sup> diffusion coefficient, the lowest charge transfer resistance and the slightest polarization. In situ X-ray diffraction characterization further reveals that during cycling, vdW gap of MoO<sub>3</sub> (II) changes periodically within a small range, indicating a stabilized crystal structure. This work shows that moderate oxygen vacancies can enhance the capacity and stabilize the structure of molybdenum trioxide cathode for LIBs, which has great potential in other cathode materials.

## 1. Introduction

Due to increasing amount of energy consumption every year, scientists have been aiming at new energies beyond traditional fossil fuels, including solar energy, tidal energy, wind energy, etc. [1]. Appropriate technologies have been well developed to obtain most of these energy sources [2]. Such kinds of energy, however, tend to be low and unstable in terms of power output, which is the main reason why they cannot be directly used [3–5]. To address this problem, low-cost energy storage technologies are required to store the transformed energy, which should feature high capacity and long cycling life [6–9].

Among the typical energy storage systems, Li-ion batteries (LIBs) stand out for their relatively large specific capacity and high operating voltage [10,11]. However, the commercialized LIBs (the cathode can only achieve 0.5 lithium transfer per transition metal) have limited specific capacity, which, during the past few decades, increases slowly due to the undesirable candidates of cathode materials [12–15]. In this

regard, considerable effort has been devoted to designing alternative cathode materials with high capacity [16–19]. The cathode materials that can store more than one electron attract much more attention.  $\alpha$ -MoO<sub>3</sub> is one of these cathode materials with high specific capacity (over 1.6 lithium per one transition metal and capacity of > 279 mAh g<sup>-1</sup>), which has been intensively studied during the past few years [20–22]. Nevertheless, according to previous researches, the capacity of  $\alpha$ -MoO<sub>3</sub> decreases rapidly because of its irreversible phase transition occurring at ~ 2.8 V [24]. In addition, the low electronic conductivity and slow reaction dynamics also limit its application [2].

So far, various methods, such as pre-intercalation and introduction of carbon materials, have been utilized to improve the electrochemical performance of  $\alpha$ -MoO<sub>3</sub> [21–24]. Qi et al. [21] synthesized the Poly (ethylene oxide)-intercalated MoO<sub>3</sub> via a hydrothermal method and found the doped material exhibits superior cycling performance and reversibility upon Li<sup>+</sup> insertion/extraction compared with pure MoO<sub>3</sub>. Similarly, Mai et al. [22] demonstrated that the lithiated MoO<sub>3</sub>

\* Corresponding author.

E-mail address: [mlq518@whut.edu.cn](mailto:mlq518@whut.edu.cn) (L. Mai).

<sup>1</sup> Guobin Zhang and Tengfei Xiong contributed equally to this work.

nanobelt displays greatly improved conductivity and slower capacity fading compared with non-lithiated  $\text{MoO}_3$  nanobelt, which explains the lower capacity fading in the former. Different from the pre-intercalation method, compositing  $\text{MoO}_3$  with graphene was realized by Dong et al. [23] to increase the conductivity as well as to reduce the stress during cycling. These methods, while improving the cycling performance of  $\text{MoO}_3$  to some extent, sacrifice the initial capacity and tend to be complicated for manufacturing. For example, for the pre-intercalation method, it is difficult to control the amount of alkali ions in the host structure during synthesis process and also, alkali ions are more likely to extract from the structure during cycling. As for the compositing modification, uniformity is not easy to achieve.

Recently, several research groups showed the critical role oxygen vacancy plays in enhancing electrochemical performance [25,26]. Li et al. [25] reported a partially reduced  $\text{MoO}_{3-x}$  via thermal reduction, which presented near theoretical capacity and improved cycling stability as the electrode material for sodium ion battery. Dunn et al. [26] proved the enhanced pseudocapacitive performance of molybdenum trioxide enabled by oxygen vacancy.

Herein, the oxygen-deficient  $\alpha\text{-MoO}_{3-x}$  is prepared via controllable plasma etching of  $\alpha\text{-MoO}_3$  nanobelts and firstly employed as the cathode material for LIB. Structural characterizations certify that after appropriate etching ( $\text{MoO}_3$  (II)), its van der Waals gap (vdW gap) expands and bandgap reduces, which further leads to lower electron transfer resistance and more efficient  $\text{Li}^+$  diffusion. As a result, less polarization, increased structural stability, more reversible interlayer/intralayer Li sites and much higher capacity are also obtained. Compared with  $\text{MoO}_3$  (II),  $\text{MoO}_3$  (III) behaves badly in terms of microstructure, BET (Brunauer-Emmet-Teller) surface area and electron transfer resistance, therefore delivering obviously lower capacity. It can be concluded that excessive etching (oxygen vacancy) has negative effect on the electrochemical performance of  $\alpha\text{-molybdenum trioxide}$ .

## 2. Experiment section

### 2.1. Material synthesis

Three samples were synthesized in this work. The first one is the original  $\alpha\text{-MoO}_3$  without reduction ( $\text{MoO}_3$  (I)), the second one ( $\text{MoO}_3$  (II)) is obtained after treating  $\text{MoO}_3$  (I) with  $\text{H}_2$  plasma etching for 10 min, and the last one ( $\text{MoO}_3$  (III)) with a longer etching time of 20 min.  $\text{MoO}_3$  (I) was synthesized via a reported hydrothermal method [24]. In detail, firstly, 4 g Mo powder was slowly added into 40 ml  $\text{H}_2\text{O}_2$  (30%) under vigorous stirring and external water cooling. Afterward the formed orange peroxomolybic acid sol was stirred for 4 h under 70 °C water bath to remove excessive  $\text{H}_2\text{O}_2$ . Then the liquid was transferred into a 50 ml Teflon-lined autoclave, which was kept in a 180 °C oven for 6 h. The obtained mixture was centrifuged with a speed of 8000 r/min for 3 min and washed by deionized water and repeated for 3 times. Finally,  $\text{MoO}_3$  (I) powder was obtained after overnight's drying in air at 70 °C.  $\text{MoO}_3$  (II) and  $\text{MoO}_3$  (III) samples were acquired via  $\text{H}_2$  plasma etching of the  $\text{MoO}_3$  (I) sample, using a PDC-MG plasma cleaner produced by Chengdu Mingheng Science & Technology Co., Ltd. The etching system was operated at an output power of 180 W (current: 200 mA, voltage: 900 V).

### 2.2. Material characterization

Scanning electron microscopy (SEM) images were recorded using a JEOL JSM-7100F microscope, with an acceleration voltage of 15 kV. The microstructure of the samples were characterized with transmission electron microscopy (JEM-2100F). Nitrogen adsorption isotherms at 77 K were measured using a Tristar II 3020 instrument. X-ray diffraction (XRD) experiments were conducted with  $\text{Cu K}\alpha$  ( $\lambda = 1.5418 \text{ \AA}$ ) using Bruker D8 Discover X-ray diffractometer under a tube current of 40 mA and a tube voltage of 40 kV. Raman spectra (50–1200  $\text{cm}^{-1}$ ) and

diffuse reflection ultraviolet-visible (DR UV-Vis) spectra (200–2500 nm) were recorded with Horiba LabRAM HR Evolution and PerkinElmer Lambda 750 S, respectively. X-ray absorption fine spectroscopy (XAFS) experiments were performed at the beamline 1W1B of Beijing Synchrotron Radiation Facility (BSRF) at Institute of High Energy Physics, Chinese Academy of Sciences. The first inflection point of the spectrum of Mo foil was used to carry out energy calibration. The X-ray absorption near edge structure (XANES) and the extended X-ray absorption fine structure (EXAFS) spectra were processed employing the software packages Athena 0.9. To highlight the high-energy oscillations, the EXAFS signal  $\chi(k)$  was weighted by  $k^3$  and then Fourier-transformed in a  $R$  range from 0 to 6.0  $\text{\AA}$ . Positron annihilation lifetime spectroscopy (PALS) was analyzed using the RGM-1/APBS-2 Trap Based Slow Positron Beam System, with a count number of 1000,000 and a time resolution of 0.230 ns. X-ray photoelectron spectroscopy (XPS) analysis was performed using Thermo Fisher Scientific ESCALAB 250Xi XPS System, with the binding energy range of 0–1350 eV.

### 2.3. Electrochemical characterization

The active material ( $\text{MoO}_3$  (I),  $\text{MoO}_3$  (II) or  $\text{MoO}_3$  (III)), acetylene black and polytetrafluoroethylene (PTFE) were mixed with a mass ratio of 6:3:1, grinded uniformly using isopropanol, and then rolled into slices, followed by drying in a 70 °C oven overnight. For the assembly of the coin cells, the acquired slice was used as the cathode, Li metal was the anode, polyethylene (PE) membrane was the separator and 1 M  $\text{LiPF}_6$  in ethylene carbonate (EC), dimethyl carbonate (DMC) and ethyl methyl carbonate (EMC) (1:1:1 by volume) served as the electrolyte. For the assembly of the in situ batteries, special battery molds were adopted, with Be window allowing the penetrating of X-ray. Both the coin and the in situ batteries were assembled in a glove box filled with argon. Electrochemical impedance spectroscopy (EIS) tests were performed using an Autolab PGSTAT302N electrochemical workstation, after 10 cycles of slow discharge-charge within 1.5–4.0 V. Cyclic voltammetry (CV) curves were obtained using CHI760E electrochemical workstation in the same voltage range, with different scan rates of 0.5, 1.0, 2.0, 5.0 and 10.0  $\text{mV s}^{-1}$ , respectively. Galvanostatic charge-discharge (GCD) tests were carried out using the LAND CT2001A battery testing system, with a current density of 1.0  $\text{A g}^{-1}$ . As for the XRD procedure setting, each single diffraction pattern was collected for 50 s without delay time at a current density of 0.2  $\text{A g}^{-1}$ .

## 3. Results and discussion

To characterize the size and shape of the synthesized products, SEM images were collected. Fig. 1(a) and (b) show that the pristine  $\alpha\text{-MoO}_3$  ( $\text{MoO}_3$  (I)) without etching forms uniform and smooth nanobelts, with a width of 300–400 nm and an average length of over 10  $\mu\text{m}$ . After etching for 10 min (Fig. 1(c) and (d)), the obtained  $\text{MoO}_3$  (II) nanobelts are slightly broken but mostly retain the original morphology, which will obtain a larger surface area. However, as the etching time increases to 20 min (Fig. 1(e) and (f)), nearly all nanobelts ( $\text{MoO}_3$  (III)) are broken into very short belts or small uneven pieces. Additionally, compared with  $\text{MoO}_3$  (II),  $\text{MoO}_3$  (III) is stacked more tightly with less space around the nanobelts. Nitrogen adsorption isotherms in Fig. S1 reveal that  $\text{MoO}_3$  (II) demonstrates the largest BET surface area (13.46  $\text{m}^2 \text{ g}^{-1}$ ), which should correspond to the shortest diffusion distance of lithium ion in the host material. And in line with the SEM results,  $\text{MoO}_3$  (III) displays obviously smaller surface area because of the close packing.

Powder XRD of the three samples are shown in Fig. 1(g)–(j). The peaks in XRD pattern of  $\text{MoO}_3$  (I) are in agreement with JCPDS No. 89–5108 and therefore  $\text{MoO}_3$  (I) can be assigned to  $Pb\bar{m}$  space group ( $\alpha\text{-MoO}_3$ ). Overall, the positions and the intensities of the XRD peaks vary with samples by the different etching time. With deeper etching, the intensity of diffraction peaks decreases, showing a more disordered

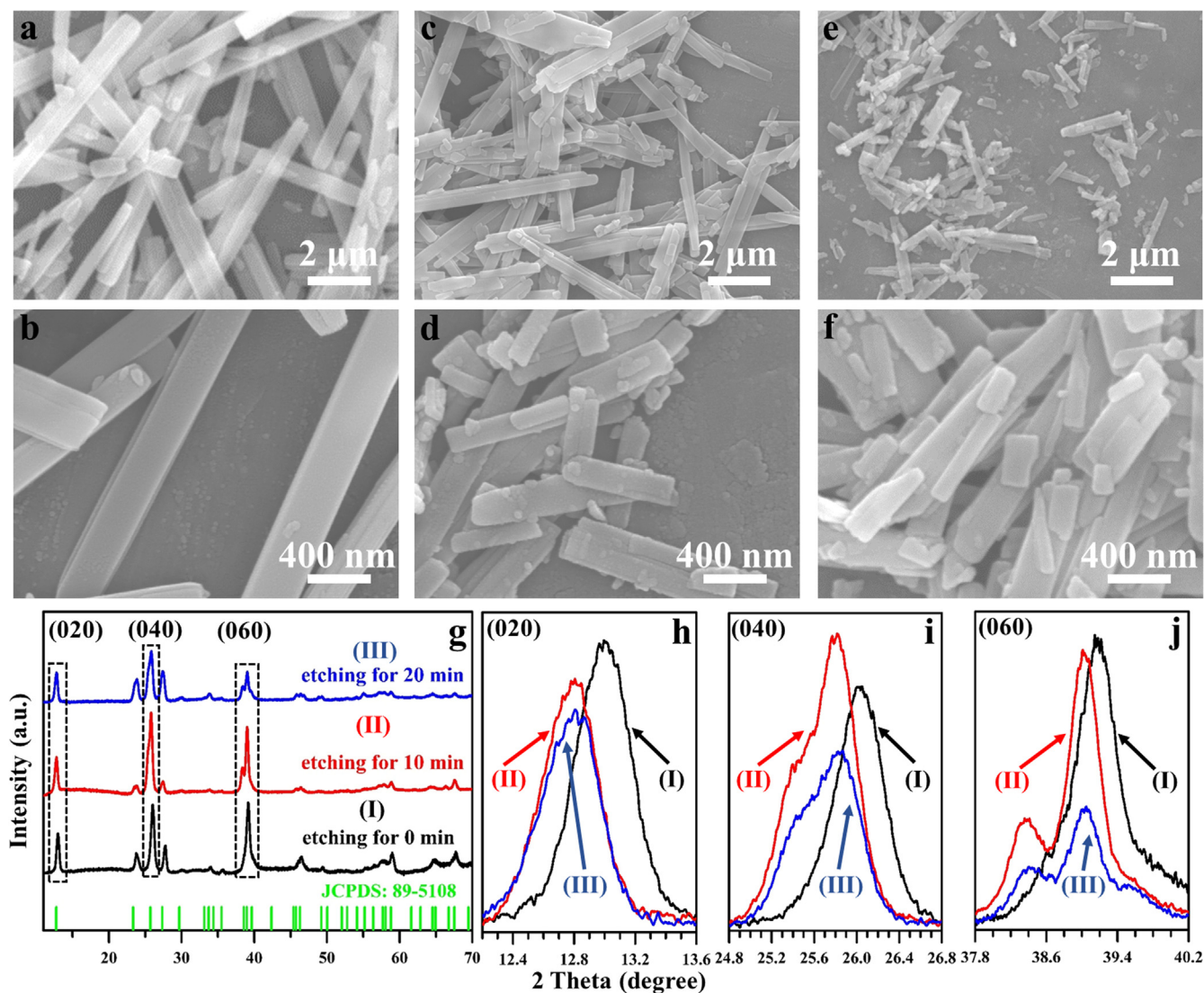


Fig. 1. Microstructure and phase analysis of the three samples: (a–b) SEM images of MoO<sub>3</sub> (I), (c–d) SEM images of MoO<sub>3</sub> (II), (e–f) SEM images of MoO<sub>3</sub> (III), (g) XRD patterns of the three samples with 2 theta range of 11–70° and (h–j) selected XRD patterns around the (020), (040) and (060) diffraction peaks.

structure. The (020), (040) and (060) peaks, which reflect vdW gap in  $\alpha$ -molybdenum trioxide, are selected to make a comparison. For all the three crystal plane reflections (Fig. 1(h)–(j)), the peaks shift to lower angle after etching, indicating an expansion of the vdW gap. Moreover, this change, on the basis of previous work, will not surprisingly speed up the ion transport in the vdW gap, which will further enhance the rate performance and cycling life of MoO<sub>3</sub> cathode. It should be noticed that when the etching time increases from 10 to 20 min, almost no shift of the three reflections or no change in the vdW gap occurs. In addition, it is pointed that etching splits the (040) and (060) peaks, with the occurrence of a small peak at a lower angle with respect to the main peak. This is probably due to greater expansion of the vdW gap near the surface of the nanobelts than that in the inside caused by etching. To characterize the local structure and morphology of the pristine and the MoO<sub>3</sub> (II), selected area electron diffraction (SAED) and high resolution transmission electron microscopy (HRTEM) were done and shown in Fig. S2 and S3, respectively. The SAED and HRTEM results show the expanding of the 040 crystal plane.

Fig. 2 shows the UV–Vis diffuse reflectance spectra of these three samples. Generally, etching greatly improves the absorbance in the whole range 200–2500 nm (Fig. 2(a)). To understand the spectra from electronic level, absorbance- $h\nu$  plots were depicted in Fig. 2(b). In the energy range of 1–2 eV, a big absorption band appears in two deficient

samples rather than in MoO<sub>3</sub> (I). Based on previous research [27], this broad band covers three transitions: the two intervalence charge transfer (IVCT) transitions located at 1.25 and 2.00 eV, respectively, and the  $d_{yz}$ - $d_{xy}$  transition located at 1.60 eV. Although deconvolution is not conducted, it is reasonable to assume that all the three transitions increase with the etching time. In this case, it can be concluded that the introduction of oxygen vacancies generates two kinds of Mo<sup>5+</sup> (one in [Mo<sup>5+</sup>O<sub>6</sub>] and another in [Mo<sup>5+</sup>O<sub>5</sub>]) in  $\alpha$ -MoO<sub>3</sub>, and this is in line with the calculation result by Dunn et al. [26].  $(ah\nu)^2$ - $h\nu$  plots are further depicted in Fig. 2(c) to calculate the bandgap [28,29], which are 3.34, 2.70 and 2.54 eV for MoO<sub>3</sub> (I), MoO<sub>3</sub> (II) and MoO<sub>3</sub> (III), respectively. As can be expected, this largely reduced bandgap will lead to an increase in the electronic conductivity, which contributes to fast charge-discharge and less polarization during the electrochemical process.

Fig. 3(a)–(c) displays the Raman spectra of the three samples with the Raman shift of 50–1200 cm<sup>-1</sup>. It can be observed that the three spectra share most vibrations except the one at 1008 cm<sup>-1</sup> (Fig. 3(a)), which, according to M. Dieterle et al. [27–29], appears as a result of oxygen vacancy. In this regard, the Raman spectra were normalized to the band at 820 cm<sup>-1</sup> to compare the bands located around 1000 cm<sup>-1</sup> (Fig. 3(b) and (c)). The results indicate that the sample by longer time etching will have higher intensity of the band at 1008 cm<sup>-1</sup>, which means more oxygen vacancies. All Raman bands appearing in the

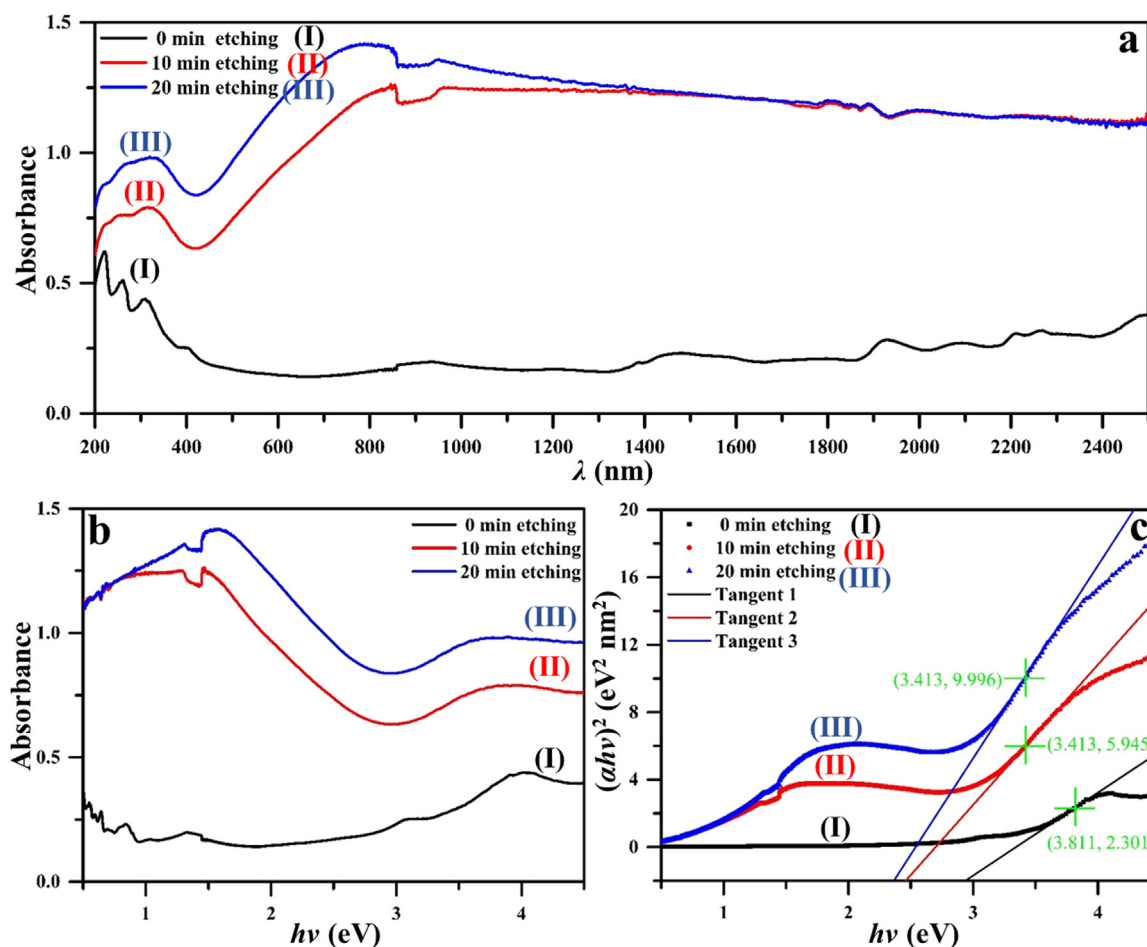


Fig. 2. UV-Vis diffuse reflectance spectra: (a) Absorbance- $\lambda$  plots of the three samples with  $\lambda$  ranging from 200 to 2500 nm, (b) absorbance- $h\nu$  plots with energy of 0.5–4.5 eV and (c)  $(ah\nu)^2$ - $h\nu$  plots in the corresponding energy range.

spectra were assigned and summarized in Table S1 according to previous researches [30–36].

XAFS analysis was employed to acquire information of the fine structure (Fig. 3(d)–(g)). The pre-edge peaks located around 20,006 eV, which represent the  $1s$ - $4d$  electron transfer in the distorted octahedron  $[\text{MoO}_6]$  [37,38], are shown in Fig. 3(e). As etching proceeds, the intensity of this peak decreases, indicating a process of oxygen loss (the loss of terminal oxygen in the  $b$  direction) [39]. For the two edge peaks located around 20,025 and 20,036 eV, they get an increase in intensity and shift to lower energy upon etching. This trend further certifies the lower average valance of Mo in the material after etching [40]. To acquire the detailed bonding and coordination information, FT-EXAFS spectra (not phase-corrected) are shown in Fig. 3(g). The peaks located in the range of 1.0–2.0 Å can be assigned to scattering of O atoms and those in the range of 2.0–4.0 Å can be assigned to Mo atoms [41,42]. Further, for all three samples, the peak located at 1.1 eV corresponds to the terminal O atom in the  $b$  direction. About this peak, two trends can be found after etching. One is the decreased peak intensity, showing less terminal O atoms at the corresponding site/distance. This phenomenon is in line with the result of the pre-edge peaks. Apart from this, etching shortens the length of Mo=O (terminal O) along  $b$  direction. Considering the Mo=O in the pristine  $\alpha$ - $\text{MoO}_3$  is already the shortest bonding between Mo and O, the etching is believed to generate a more distorted structure.

To investigate the oxygen vacancies from a macroscopic perspective, PALS and XPS spectra of the pristine and the oxygen-deficient samples were collected. The PALS spectra are displayed in Fig. S4. In the distribution versus lifetime, the counts of  $\text{MoO}_3$  (II), on the whole,

show a slight shift to higher lifetime compared with those of  $\text{MoO}_3$  (I). Accordingly, the positron annihilation lifetime was calculated to be 0.2965 and 0.3095 ns for  $\text{MoO}_3$  (I) and  $\text{MoO}_3$  (II), respectively (Table S2) [43]. This attests the lower electron cloud density in  $\text{MoO}_3$  (II), which is a prominent influence brought by oxygen vacancies [44]. Mo 3d XPS results of the oxygen-deficient samples are shown in Fig. 4(a) and (b). In the energy range of 229–240 eV, four distinct peaks can be observed, indicating the existence of  $\text{Mo}^{5+}$  (near 231.7 and 234.8 eV) and  $\text{Mo}^{6+}$  (near 233.1 and 236.2 eV) [45]. After peak-fit processing, the formula is calculated to be  $\text{MoO}_{2.912}$  and  $\text{MoO}_{2.870}$  for  $\text{MoO}_3$  (I) and  $\text{MoO}_3$  (II), respectively.

The electrochemical measurement results shown in Fig. 5 are discussed to investigate the lithium storage performance of the synthesized materials. Comparison of electrochemical impedance spectroscopy (EIS) of the three samples is conducted in Fig. 5(c). After etching,  $\text{Li}^+$  diffusion in  $\text{MoO}_3$  (II) and  $\text{MoO}_3$  (III) becomes faster, characterized by the larger slope of the line part. In addition, the charge transfer resistance of  $\text{MoO}_3$  (II) becomes smaller while that of  $\text{MoO}_3$  (III) grows. Considering the EIS, SEM and BET results,  $\text{MoO}_3$  (III) is likely to exhibit lower performance (which is verified in the following part) and hence is excluded in the CV measurement. Voltammetric sweeps of  $\text{MoO}_3$  (I) and  $\text{MoO}_3$  (II) were conducted in the voltage range of 1.5–4.0 V, at different scan rates of 0.5, 1.0, 2.0, 5.0 and  $10 \text{ mV s}^{-1}$ , respectively (shown in Fig. 5(a) and (b)). For  $\text{MoO}_3$  (I), two pairs of redox peaks 2.69/2.05 V and 3.45/2.71 V can be clearly observed at a low scan rate of  $1.0 \text{ mV s}^{-1}$ , corresponding to the interlayer Li storage sites (vdW gap) and the intralayer sites, respectively (Fig. S5) [45]. When the scan rate increases to 5 or  $10 \text{ mV s}^{-1}$ , the main CV peak (interlayer sites) is incomplete, due

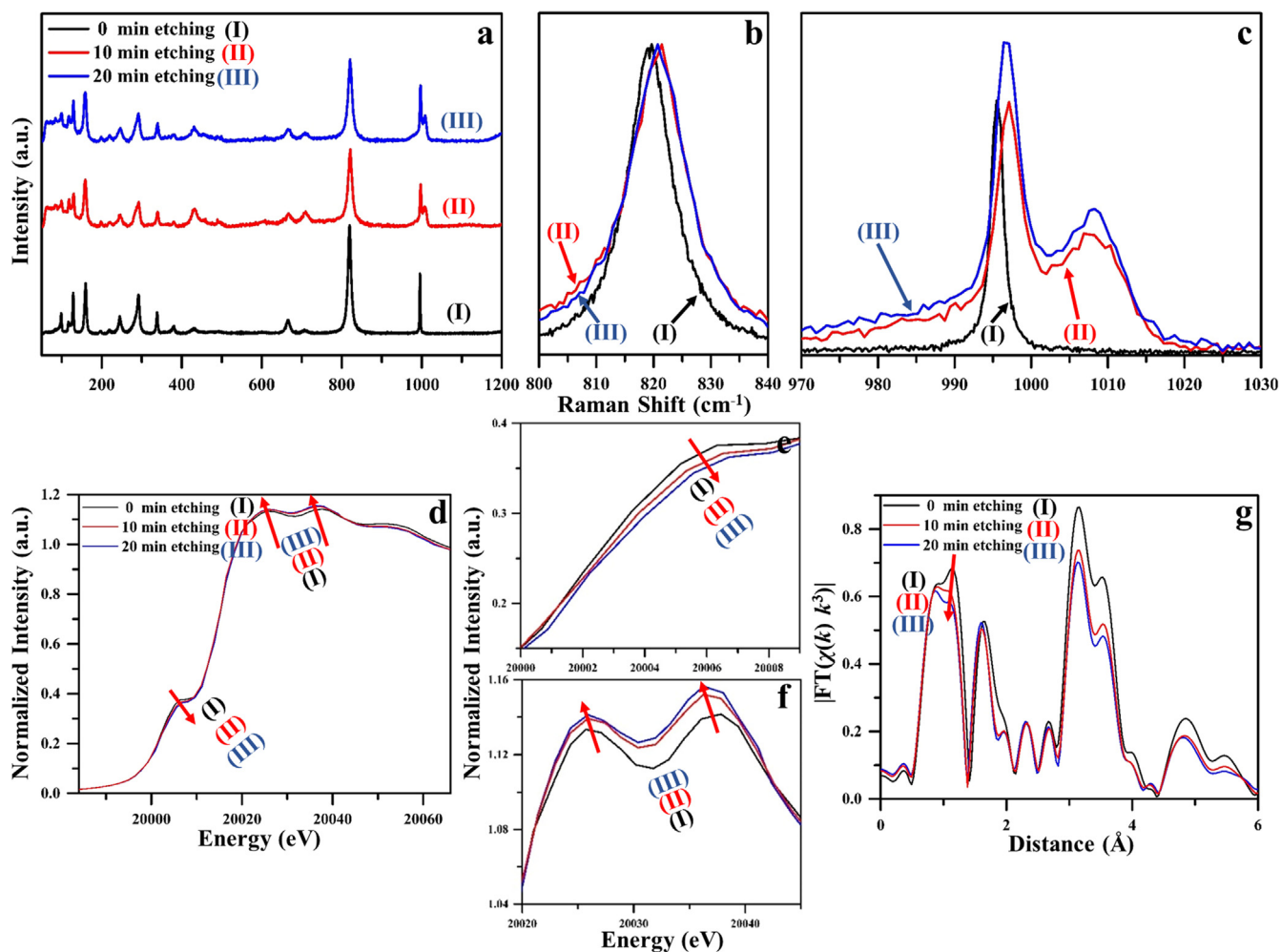


Fig. 3. Raman spectra and XAFS spectra: (a) Raman spectra (not normalized) with the Raman shift of 50–1200  $\text{cm}^{-1}$ , (b–c) normalized Raman spectra to the band at 820  $\text{cm}^{-1}$  in the energy range 800–840  $\text{cm}^{-1}$  and 970–1030  $\text{cm}^{-1}$ , respectively, (d) XANES spectra of Mo-K edge, (e) the magnified plots of the pre-edge peaks, (f) the magnified plots of the edge peaks and (g) the corresponding FT-EXAFS spectra in  $R$  space.

to the increased polarization. As a result, much more Li storage sites become inactive in the electrochemical process. In comparison,  $\text{MoO}_3$  (II) displays better performance in the CV test. Firstly, CV peaks for both sites are more distinct (larger peak current and integral area), indicating improved reversibility of the de-intercalation reaction and increased active Li storage sites. Secondly, with respect to the reduction

peaks,  $\text{MoO}_3$  (II) shows smaller polarization and more complete peak shape, probably achieved by the reduced bandgap (increased electronic conductivity). Thirdly, considering the peak current only,  $\text{MoO}_3$  (II) shows a much faster kinetic process. To demonstrate this specifically,  $\text{Li}^+$  diffusion coefficients ( $D_{\text{Li}}$ ) were calculated via the Randles–Sevcik equation [46], taking the interlayer site peak as the example (Table 1

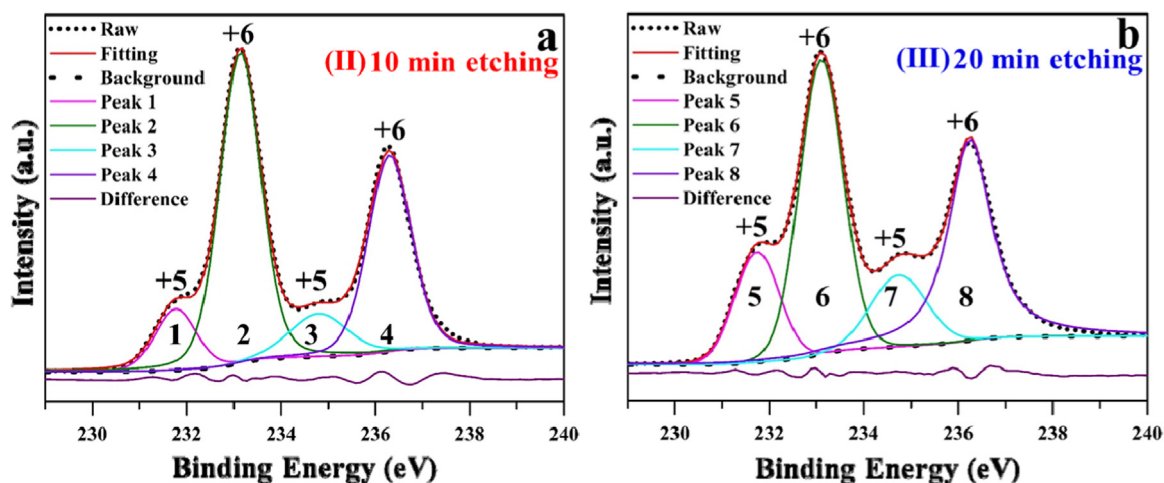


Fig. 4. Mo 3d XPS spectra of the two oxygen-deficient samples: (a)  $\text{MoO}_3$  (II) and (b)  $\text{MoO}_3$  (III).

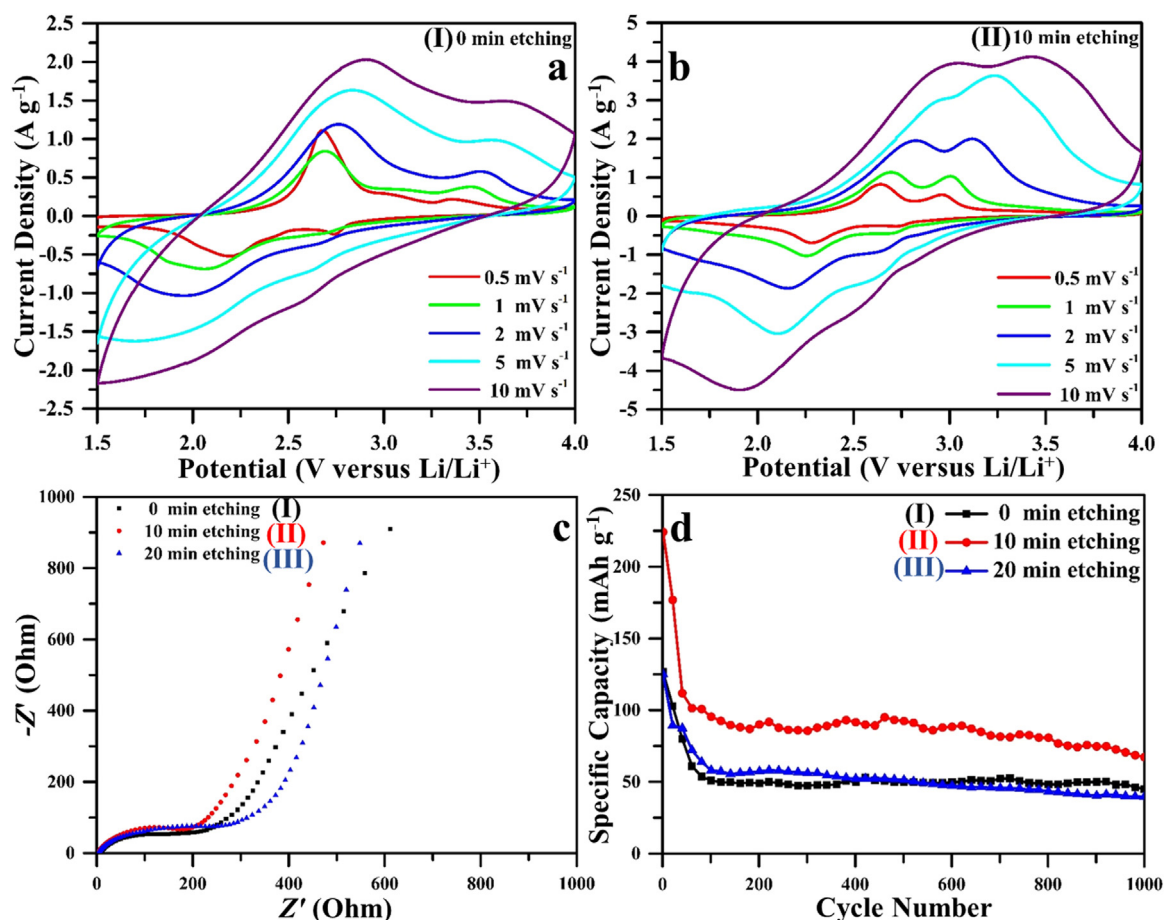


Fig. 5. Electrochemical characterizations: (a–b) voltammetric sweeps of MoO<sub>3</sub> (I) and MoO<sub>3</sub> (II), respectively, (c) Nyquist plots of the three samples and (d) cycling performance at 1 A g<sup>-1</sup>.

Table 1

$D_{Li}$  calculated from the oxidation peaks (unit: m<sup>2</sup> s<sup>-1</sup>).

	1 mV s <sup>-1</sup>	2 mV s <sup>-1</sup>	5 mV s <sup>-1</sup>	Average
MoO <sub>3</sub> (I)	$4.19 \times 10^{-13}$	$4.19 \times 10^{-13}$	$3.15 \times 10^{-13}$	$3.84 \times 10^{-13}$
MoO <sub>3</sub> (II)	$7.59 \times 10^{-13}$	$1.13 \times 10^{-12}$	$1.09 \times 10^{-12}$	$9.93 \times 10^{-13}$

Table 2

$D_{Li}$  calculated from the reduction peaks (unit: m<sup>2</sup> s<sup>-1</sup>).

	1 mV s <sup>-1</sup>	2 mV s <sup>-1</sup>	5 mV s <sup>-1</sup>	Average
MoO <sub>3</sub> (I)	$2.79 \times 10^{-13}$	$3.16 \times 10^{-13}$	$3.12 \times 10^{-13}$	$3.02 \times 10^{-13}$
MoO <sub>3</sub> (II)	$6.27 \times 10^{-13}$	$1.03 \times 10^{-12}$	$1.09 \times 10^{-12}$	$9.16 \times 10^{-13}$

and Table 2). Results show that  $D_{Li}$  in MoO<sub>3</sub> (II) is about three times the value of that in MoO<sub>3</sub> (I), whether the reduction or oxidation process. Each of the above three factors will contribute to the actual capacity of  $\alpha$ -MoO<sub>3</sub> ( $\alpha$ -MoO<sub>3-x</sub>) as the cathode material for LIB.

Fig. 5(d) illustrates the long-term cycling performance of the three samples at 1.0 A g<sup>-1</sup>. In the initial cycle, the discharge capacities of MoO<sub>3</sub> (I), MoO<sub>3</sub> (II) and MoO<sub>3</sub> (III) are 126.7, 224.2 and 125.1 mAh g<sup>-1</sup>, respectively. In the next 100 cycles, all three samples witness a fast decrease in capacity, due to the destruction of the crystal structure. As for following cycles, all the capacities decline slowly, which are 45.1, 67.3 and 39.5 mAh g<sup>-1</sup>, respectively in the 1000th cycle. The fact that MoO<sub>3</sub> (II) delivers much higher capacity than MoO<sub>3</sub> (I) should be ascribed to the improved reversibility of Li<sup>+</sup> intercalation/extraction. Moreover, as expected, MoO<sub>3</sub> (III) shows the worst cycling

performance, which can be explained by the collapse of the nanostructure. To further evaluate the electrochemical properties, rate performances at current densities of 0.1, 0.2, 0.5, 1, 2 and 5 A g<sup>-1</sup> of the samples prepared at different etching time are presented in Fig. S6. The MoO<sub>3</sub> (II) delivers the highest specific capacity and best rate capability, while the MoO<sub>3</sub> (I) shows the lowest.

To further analyze the valence state of molybdenum in the MoO<sub>3</sub> (II) after the first cycle, ex situ XPS was done shown in Fig. S7. The result shows that after discharge-charge process, there is still little V<sup>5+</sup> in the material due to the oxygen-deficient. Raman spectrum of the MoO<sub>3</sub> (II) after the first cycle shown in Fig. S8. The result shows that the main vibration modes of MoO<sub>3</sub> are nearly disappeared while the Raman shift region that can represent the oxygen-deficient still with relatively high intensity. The Raman result proves that there may still be oxygen-deficient after discharge/charge process in the material.

To give insight into the structure evolution, in situ XRD patterns of the cathode materials were recorded during charge-discharge cycling at 0.4 A g<sup>-1</sup>. The 1D patterns were transformed into 2D patterns for a better view, and the (020) diffraction was chosen because of its relatively high intensity (Fig. 6). Upon Li<sup>+</sup> intercalation, the peak shifts to lower angle, indicating an expansion of the vdW gap. As for the charge process, the change is reversed. This result is similar to that of most cathode materials for LIB. In the first 14th cycles, the position of (020) peak of MoO<sub>3</sub> (II) changes periodically, with a variation less than 2 degrees in a given cycle (Fig. 6(b)). For different cycles of the same voltage, this position has negligible shift. This phenomenon demonstrates that the crystal structure of MoO<sub>3</sub> (II) is stabilized and the vdW gap displays a periodical variation during the electrochemical process, which can further provide evidence for the high reversibility of Li<sup>+</sup>

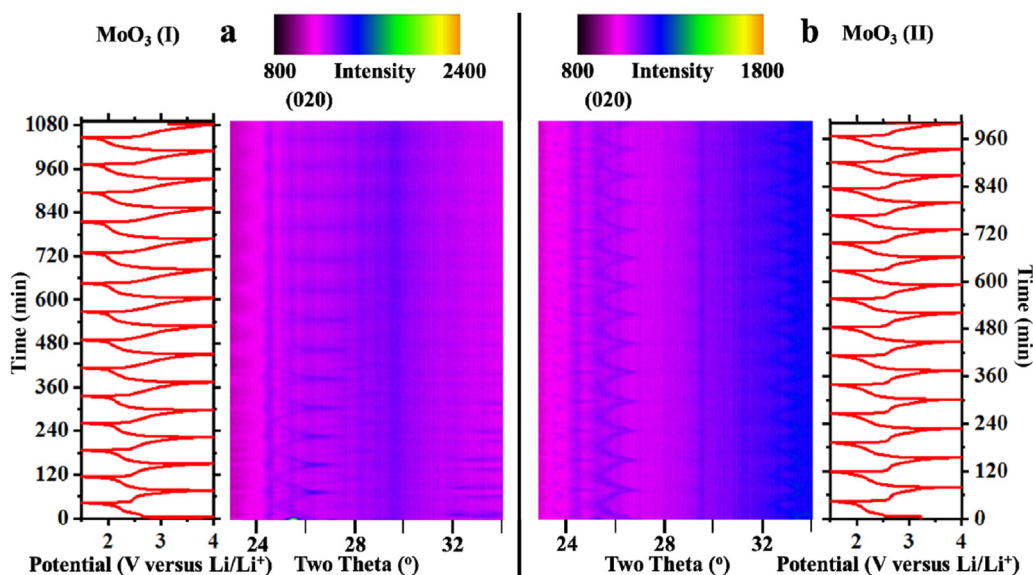


Fig. 6. *In situ* XRD test results while cycling the batteries at 0.4 A g<sup>-1</sup>: (a) MoO<sub>3</sub> (I) and (b) MoO<sub>3</sub> (II).

intercalation/extraction. In comparison with MoO<sub>3</sub> (II), MoO<sub>3</sub> (I) exhibits much lower performance when it comes to structural stability. On the one hand, the (020) peak of MoO<sub>3</sub> (I) shifts to higher angle regarding different cycles, suggesting a gradually contracted vdW gap and reduced Li storage sites. On the other hand, the intensity of (020) diffraction decrease as the cycling goes, indicating that the structure is being destroyed in Li<sup>+</sup> intercalation/extraction. The *in situ* test results fit well with the material characterization and the electrochemical test results.

#### 4. Conclusions

In this work, two kinds of H<sub>2</sub> plasma-induced α-MoO<sub>3-x</sub> (MoO<sub>3</sub> (II) and MoO<sub>3</sub> (III)) were prepared on the basis of the pristine α-MoO<sub>3</sub> (MoO<sub>3</sub> (I)), with the etching time of 10 and 20 min, respectively. Advanced material characterizations and electrochemical tests are performed to investigate the crystal structure and the Li storage performance. After plasma etching, both two oxygen-deficient molybdenum trioxides obtain a largely reduced bandgap and an expanded vdW gap. Electrochemical tests demonstrate that MoO<sub>3</sub> (II) possesses the largest Li<sup>+</sup> diffusion coefficient, the lowest charge transfer resistance and the slightest polarization during the electrochemical process. This is why MoO<sub>3</sub> (II) displays much higher capacity than MoO<sub>3</sub> (I) and MoO<sub>3</sub> (III) do. *In situ* XRD further reveals that during cycling, the variation of vdW gap of MoO<sub>3</sub> (II) is small and periodical, presenting a stabilized crystal structure. In summary, this work shows the role that moderate oxygen vacancies play in enhancing the electrochemical performance of molybdenum trioxide cathode material for LIB. This strategy can further help optimize the electrochemical performance of cathode materials.

#### Acknowledgements

This work was supported by the National Natural Science Fund for Distinguished Young Scholars (51425204), the National Natural Science Foundation of China (51521001), the National Key Research and Development Program of China (2016YFA0202603, 2016YFA0202604), the Programme of Introducing Talents of Discipline to Universities (B17034), the Yellow Crane Talent (Science & Technology) Program of Wuhan City and the Fundamental Research Funds for the Central Universities (WUT: 2017III009, 2017III005, 2017-YB-005).

#### Appendix A. Supporting information

Supplementary data associated with this article can be found in the online version at <http://dx.doi.org/10.1016/j.nanoen.2018.04.075>.

#### References

- [1] J. Liu, *Adv. Funct. Mater.* 23 (2013) 924–928.
- [2] D. Larcher, J.M. Tarascon, *Nat. Chem.* 7 (2015) 19–29.
- [3] J.M. Tarascon, M. Armand, *Nature* 414 (2001) 359–367.
- [4] M.S. Whittingham, *Chem. Rev.* 104 (2004) 4271–4301.
- [5] A.S. Arico, P. Bruce, B. Scrosati, J.M. Tarascon, W. van Schalkwijk, *Nat. Mater.* 4 (2005) 366–377.
- [6] C.K. Chan, H.L. Peng, G. Liu, K. McIlwrath, X.F. Zhang, R.A. Huggins, Y. Cui, *Nat. Nanotechnol.* 3 (2008) 31–35.
- [7] S.L. Xia, J.F. Ni, S.V. Savilov, L. Li, *Nano Energy* 45 (2018) 407–412.
- [8] J.F. Ni, G.B. Wang, J. Yang, D.L. Gao, J.T. Chen, L.J. Gao, *J. Power Sources* 247 (2014) 90–94.
- [9] C.J. Chen, Y. Zhang, Y.J. Li, J.Q. Dai, J.W. Song, Y.G. Yao, Y.H. Gong, I. Kierzewski, J. Xie, L.B. Hu, *Energy Environ. Sci.* 10 (2017) 538–545.
- [10] M. Armand, J.M. Tarascon, *Nature* 451 (2008) 652–657.
- [11] P.G. Bruce, B. Scrosati, J.M. Tarascon, *Angew. Chem. Int. Ed.* 47 (2008) 2930–2946.
- [12] J.B. Goodenough, K.S. Park, *J. Am. Chem. Soc.* 135 (2013) 1167–1176.
- [13] Y.Q. Wang, Z.Z. Yang, Y.M. Qian, L. Gu, H.S. Zhou, *Adv. Mater.* 27 (2015) 3915–3920.
- [14] J.F. Ni, G.B. Wang, J. Yang, D.L. Gao, J.T. Chen, L.J. Gao, *J. Power Sources* 247 (2014) 90–94.
- [15] S.D. Fu, J.F. Ni, Y. Xu, Q. Zhang, L. Li, *Nano Lett.* 16 (2016) 4544–4551.
- [16] M.R. Palacin, *Chem. Soc. Rev.* 38 (2009) 2565–2575.
- [17] Y.K. Sun, S.T. Myung, B.C. Park, J. Prakash, I. Belharouak, K. Amine, *Nat. Mater.* 8 (2009) 320–324.
- [18] V. Etacheri, R. Marom, R. Elazari, G. Salitra, D. Aurbach, *Energy Environ. Sci.* 4 (2011) 3243–3262.
- [19] J.F. Ni, W. Wang, C. Wu, H. Liang, J. Maier, Y. Yu, *Adv. Mater.* 29 (2016) 1605607.
- [20] X.L. Ji, L.F. Nazar, *J. Mater. Chem.* 20 (2010) 9821–9826.
- [21] N.A. Chernova, M. Roppolo, A.C. Dillon, M.S. Whittingham, *J. Mater. Chem.* 19 (2009) 2526–2552.
- [22] Y. Yang, M.T. McDowell, A. Jackson, J.J. Cha, S.S. Hong, Y. Cui, *Nano Lett.* 10 (2010) 1486.
- [23] T. Tsumura, *Solid State Ion.* 104 (1997) 183–189.
- [24] Y. Iriyama, *Solid State Ion.* 135 (2000) 95–100.
- [25] Y.Y. Qi, W. Chen, L.Q. Mai, Q.Y. Zhu, A.P. Jin, *Int. J. Electrochem. Sci.* 1 (2006) 317–323.
- [26] L.Q. Mai, B. Hu, W. Chen, Y.Y. Qi, C.S. Lao, R.S. Yang, Y. Dai, Z.L. Wang, *Adv. Mater.* 19 (2007) 3712–3716.
- [27] Y.F. Dong, S. Li, H.M. Xu, M.Y. Yan, X.M. Xu, X.C. Tian, Q. Liu, L.Q. Mai, *Phys. Chem. Chem. Phys.* 15 (2013) 17165–17170.
- [28] Y.F. Dong, X.M. Xu, S. Li, C.H. Han, K.N. Zhao, L. Zhang, C.J. Niu, Z. Huang, L.Q. Mai, *Nano Energy* 15 (2015) 145–152.
- [29] Y.F. Li, D.D. Wang, Q.Y. An, B. Ren, Y.G. Rong, Y. Yao, *J. Mater. Chem. A* 4 (2016) 5402–5405.
- [30] H.S. Kim, J.B. Cook, H. Lin, J.S. Ko, S.H. Tolbert, V. Ozolins, B. Dunn, *Nat. Mater.* 16 (2017) 454–460.

- [31] M. Dieterle, G. Weinberg, G. Mestl, *Phys. Chem. Chem. Phys.* 4 (2002) 812–821.  
 [32] M.A. Butler, *J. Appl. Phys.* 48 (1977) 1914–1920.  
 [33] L. Cheng, M.W. Shao, X.H. Wang, H.B. Hu, *Chem. -Eur. J.* 15 (2009) 2310–2316.  
 [34] M.F. Daniel, B. Desbat, J.C. Lassegues, B. Gerand, M. Figlarz, *J. Solid State Chem.* 67 (1987) 235–247.  
 [35] L. Seguin, M. Figlarz, R. Cavagnat, J.C. Lassègues, *Spectrochim. Acta A* 51 (1995) 1323–1344.  
 [36] G. Mestl, N.F.D. Verbruggen, E. Bosch, H. Knözinger, *Langmuir* 12 (1996) 2961–2968.  
 [37] M.A. Py, P.E. Schmid, J.T. Vallin, *Il Nuovo Cim.* 38 (2007) 271–279.  
 [38] Y.N. Zhou, J. Ma, E.Y. Hu, X.Q. Yu, L. Gu, K.W. Nam, L.Q. Chen, Z.X. Wang, X.Q. Yang, *Nat. Commun.* 5 (2014) 5381.  
 [39] K. Yokoi, N. Matsubayashi, T. Miyanaaga, I. Watanabe, K. Murata, S. Ikeda, *Chem. Lett.* 16 (1987) 1453–1456.  
 [40] A. Michailovski, J.D. Grunwaldt, A. Baiker, R. Kiebach, W. Bensch, G.R. Patzke, *Angew. Chem. Int. Ed.* 44 (2005) 5643–5647.  
 [41] T. Ressler, O. Timpe, T. Neisius, J. Find, G. Mestl, M. Dieterle, R. Schlögl, *J. Catal.* 191 (2000) 75–85.  
 [42] L.L. Jin, X.S. Zheng, W. Liu, L.L. Cao, Y.J. Cao, T. Yao, S.Q. Wei, *J. Mater. Chem. A* 5 (2017) 12022–12026.  
 [43] Y.W. Zhou, J.J. Li, C.S. Yin, W.F. Mao, J.C. Wang, C.Q. He, *Phys. Rev. A* 94 (2016) 022513.  
 [44] C.S. Yin, L.T. Wang, J.J. Li, Y.W. Zhou, H.N. Zhang, P.F. Fang, C.X. He, *Phys. Chem. Chem. Phys.* 19 (2017) 15953–15961.  
 [45] X. Wei, L.F. Jiao, J.L. Sun, S.C. Liu, H.T. Yuan, *J. Solid State Electrochem.* 14 (2009) 197–202.  
 [46] M.Y. Yan, G.B. Zhang, Q.L. Wei, X.C. Tian, K.N. Zhao, Q.Y. An, L. Zhou, Y.T. Zhao, C.J. Niu, W.H. Ren, L. He, L.Q. Mai, *Nano Energy* 22 (2016) 406–413.



**Liang He** is an associate professor of the State Key Laboratory of Advanced Technology for Materials Synthesis and Processing at Wuhan University of Technology. He received his Ph.D. degree from Tohoku University (Japan) in 2013. His current research interests include the microfabrication and characterizations of micro/nanostructures and devices for applications in MEMS (Micro Electro Mechanical Systems).



**Xiaobin Liao** received his M.S. degree in Department of Materials Science and Engineering from Wuhan University of Technology in 2018. He is currently working toward the Ph.D. degree. His current research involves the energy storage/conversion materials, nanoscale devices and DFT calculation.



**Chunqing He** is a Professor in the School of Physics and Technology, Wuhan University. He received his BS in Physics from Wuhan University in 1995 and his PhD in Physics from Fudan University in 2001. After 7 years postdoctoral research in Japan, he started his independent academic career at Wuhan University, working on physics and material science.



**Chongshan Yin** received his B.S. degree from Dalian University of Technology. He is currently working toward the Ph.D. degree and his current research interests focus on the physical chemistry.



**Haining Zhang** started to study chemistry at Wuhan University in 1990. He joined Prof. Ruhe's group at University of Freiburg in 1999 and received his doctor degree in 2003. After two postdoctoral positions at UC Santa Barbara and University of Sheffield, he was appointed as professor in 2007, at Wuhan University of Technology, working on polymeric materials for energy-related devices.



**Guobin Zhang** received his B.S. degree from Inner Mongolia University of Science & Technology in 2014. He got his M.S. degree in Department of Materials Science and Engineering from Wuhan University of Technology in 2016 and he is currently working toward the Ph.D. Degree in Wuhan University of Technology. His current research focuses on in situ characterization.



**Tengfei Xiong** is a senior student in International School of Materials Science and Engineering at Wuhan University of Technology. His current research is focused on energy storage.



**Mengyu Yan** received his Ph.D. from the State Key Laboratory of Advanced Technology for Materials Synthesis and Processing, Wuhan University of Technology in 2016, under the supervision of Prof. Liqiang Mai. Currently, he is a WRF innovation postdoctoral fellow at the Materials Science and Engineering department, University of Washington. His current research involves the energy storage/conversion materials and nanoscale devices.



**Liqiang Mai** is Chair Professor of Materials Science and Engineering at Wuhan University of Technology (WUT). He is Cheung Kong Scholar Chair Professor and the winner of the National Natural Science Fund for Distinguished Young Scholars. His current research interests focus on new nanomaterials for electrochemical energy storage and micro/nano energy devices. He received his Ph.D. degree from WUT in 2004. He carried out his postdoctoral research in the laboratory of Prof. Zhonglin Wang at Georgia Institute of Technology in 2006–2007 and worked as advanced research scholar in the laboratory of Prof. Charles M. Lieber at Harvard University in 2008–2011. He worked as advanced research scholar in the laboratory of Prof. Peidong Yang at University of California, Berkeley in 2017.

Yang at University of California, Berkeley in 2017.